On Modeling Air/Space-Borne Radar Returns in the Melting Layer

Liang Liao
Goddard Earth Sciences & Technology/Caelum Research Corp.,
Code 975, NASA/GSFC, Greenbelt, MD 20771

Robert Meneghini
Code 975, NASA/GSFC, Greenbelt, MD 20771

Submitted to
IEEE Transactions on Geoscience and Remote Sensing

Revised in February 2005

Corresponding author information:

Dr. Liang Liao
Goddard Earth Sciences & Technology/Caelum Research Corp.
Code 975
NASA/Goddard Space Flight Center
Greenbelt, MD 20771

301-614-5718 (phone)
301-614-5558 (fax)
Email: lliao@neptune.gsfc.nasa.gov

Abstract

The bright band is the enhanced radar echo associated with the melting of hydrometeors in stratiform rain where the melting process usually occurs below 0 ^{0}C isotherm over a distance of about 500m. To simulate this radar signature, a scattering model of melting snow is proposed in which the fractional water content is prescribed as a function of the radius of a spherical mixed-phase particle consisting of air, ice and water. The model is based on the observation that melting starts at the surface of the particle and then gradually develops towards the center. To compute the scattering parameters of a non-uniform melting particle, the particle is modeled as a sphere represented by a collection of 64^3 cubic cells of identical size where the probability of water at any cell is prescribed as a function of the radius. The internal field of the particle, used for deriving the effective dielectric constant, is computed by the Conjugate Gradient and Fast Fourier Transform (CGFFT) numerical methods. To make computations of the scattering parameters more efficient, a multi-layer stratified-sphere scattering model is introduced after demonstrating that the scattering parameters of the non-uniformly melting particle can be accurately reproduced by the stratified sphere. In conjunction with a melting layer model that describes the melting fractions and fall velocities of hydrometeors as a function of the distance from the 0 ^{0}C isotherm, the stratified-sphere model is used to simulate the radar bright band profiles. These simulated profiles are shown to compare well with measurements from the Precipitation Radar (PR) aboard the Tropical Rainfall Measuring Mission (TRMM) satellite and a dual-wavelength airborne radar. The results suggest that the proposed model of a melting snow particle may be useful in studying the characteristics of the bright-band in particular and mixed-phase hydrometeors in general.

Index Terms: Air/Space-borne radar, effective dielectric constant, radar bright band, melting layer, electric scattering.

I. INTRODUCTION

The bright band, a layer of enhanced radar reflectivity, is often observed in stratiform rain in the layer where the snow melting process takes place. The primary cause of the enhancement is a rapid increase in the dielectric constant of hydrometeors at the top of the melting layer. After reaching a maximum, the reflectivity decreases because of an increase in particle velocities and a decrease in the effective particle size. Understanding the microphysical properties of melting hydrometeors and their electric scattering and propagation effects is crucial in estimating parameters of the precipitation from space-borne radar and radiometer measurements [1-4], such as the Tropical Rainfall Measuring Mission (TRMM) Precipitation Radar (PR) and the TRMM Microwave Imager (TMI). Simulations of radar profiles of the bright band generally require two models: a meteorological melting layer model that describes the complex physical phenomena that couples the particle melting with the dynamical and thermodynamical processes within the melting layer; a particle scattering model of melting snow that characterizes the scattering and propagation properties of hydrometeors at microwave and millimeter wavelengths. While both models are important for investigation of the melting layer, our focus of this study is on the analysis of the particle scattering model. This involves specifying the distribution of water within the particle and a method for computing the scattering and absorption properties of the melting snow.

An accurate description of the dielectric constant of melting hydrometeors at microwave frequencies is essential to effectively calculate the radar reflectivity factor. Because of the complex nature of the melting process and lack of experimental data on the effective dielectric constant of the melting snow, computations of the scattering properties of melting hydrometeors rely on particle melting models. Two melting models often appear in the literature: one is the

uniformly mixed model where the water fraction is constant (uniform mixture) throughout the particle; another is the two-layer concentric-sphere model where the water is confined to the outer shell and snow to the inner core. The most commonly used formulas for the effective dielectric constant for uniformly melting snow are those of Maxwell-Garnett [5] and Bruggeman [6]. However it is physically unclear as to which formula should be used and in the case of Maxwell-Garnett formulation, which component should be selected as matrix or inclusion in the mixture. As will be shown later, this choice is critical in the determination of the dielectric constant of the melting snowflake as it leads to significant differences in the simulated radar profiles of the melting region.

Meneghini and Liao [7] have proposed an expression for the effective dielectric constant, ε_{eff}, for ice/snow-water mixtures for wavelengths between 3 and 28 mm in terms of the fractional water volume and wavelength, based on a parameterization of the numerical results obtained from realizations of mixed-phase hydrometeors composed of air, ice and water. The results are derived under the assumption that the air, ice and water are mixed homogeneously. However, observations [8, 9] indicate that the melting of snow aggregates and graupel starts at the surface of the particle and progresses towards the center. It is therefore reasonable to model the melting particle as a non-uniform mixture with a water fraction that decreases toward the center. In this paper, we focus on the discussion of effective dielectric constant of melting hydrometeors by constructing a non-uniformly melting model of snow, followed by a simulation of the radar bright band and comparisons to the air/space-borne radar measurements.

Section II of the paper gives a derivation of ε_{eff} and a discussion on its range of validity. Computations of ε_{eff} are made in Section III for snow (air-ice mixture) and melting snow (snow-water mixture) where the fractional ice and water contents are prescribed as a function of radius

of the air-ice and snow-water spheres. In Section IV a multi-layer stratified-sphere model is constructed with scattering characteristics similar to those obtained from the CGFFT scattering model. Simulations of the radar bright-band profiles for the cases of TRMM PR and dual-wavelength airborne radar are made in Section V by using a stratified-sphere model in which the effective dielectric constant for a uniform mixture is used at each layer. A summary of the study is given in Section VI.

II. THEORETICAL BACKGROUND OF ε_{eff}

Let $\mathbf{E}(\mathbf{r}, \lambda)$ and $\mathbf{D}(\mathbf{r}, \lambda)$ be the local electric and dielectric displacement fields at free-space wavelength λ, satisfying

$$\boldsymbol{D}(\boldsymbol{r},\lambda) = \varepsilon(\boldsymbol{r},\lambda)\boldsymbol{E}(\boldsymbol{r},\lambda). \tag{1}$$

In view of the local constitutive law described by the above equation, the bulk effective dielectric constant is defined as the ratio of the volume averages of **D** and **E** fields of a composite material [10]. This relationship can be written as

$$\varepsilon_{eff} \iiint_V \boldsymbol{E}(\boldsymbol{r},\lambda)dv = \iiint_V \boldsymbol{D}(\boldsymbol{r},\lambda)dv, \tag{2}$$

where V is the entire volume of the particle. If the particle, composed of two materials with dielectric constants ε_1 and ε_2, is approximated by N small equi-volume elements, the ε_{eff} can be written as

$$\varepsilon_{eff} = \left(\varepsilon_1 \sum_{j\in M_1} E_j + \varepsilon_2 \sum_{j\in M_2} E_j\right) \Big/ \left(\sum_{j\in M_1} E_j + \sum_{j\in M_2} E_j\right). \tag{3}$$

The notation $\sum_{j\in M_1}$ and $\sum_{j\in M_2}$ denotes a summation over all volume elements comprising materials 1 and 2, respectively. Dividing both numerator and denominator by N in (3), and

letting f_1 and f_2 be the fractional volumes of component 1 and 2, respectively, ε_{eff} can be expressed by

$$\varepsilon_{eff} = \left(\varepsilon_1 f_1 \langle E_1 \rangle + \varepsilon_2 f_2 \langle E_2 \rangle\right) \Big/ \left(f_1 \langle E_1 \rangle + f_2 \langle E_2 \rangle\right), \tag{4}$$

where $f_1 + f_2 = 1$, and <E> represents mean field. ε_{eff} is generally a tensor for arbitrary shapes of the particles and inclusions, but is a scalar for a sphere if the mixing ratio is only a function of radius.

In our study, the internal fields appearing on the right-hand sides of (3) and (4) are computed by the CGFFT numerical procedure in which the volume enclosing the total particle is divided in 64×64×64 identical cells with a grid size small enough so that each component of the electric field is constant within it. The CGFFT method is a numerical technique that is efficiently used to solve the electric field integral equation derived from Maxwell equations. To find solutions to the large set of simultaneous linear equations obtained from the integral equation, an iterative procedure based on the Conjugate Gradient (CG) method is employed; the Fast Fourier Transform (FFT) is then used to compute the summation that is in the form of a convolution. The CGFFT scheme is versatile and can be utilized to generate scattering coefficients for objects of arbitrary geometry and material composition. It is also computationally efficient because of the FFT technique. Although the accuracy and applicable range of the CGFFT, like other numerical approaches, depend on electrical sizes of particles, it is generally accurate in the microwave range for particles with size parameters ($2\pi a/\lambda$, where a is the particle radius) of up to 5 for uniform water and up to 10 for uniform ice spheres if the particles are represented by 64×64×64 elements. The range of applicability for the CGFFT can be improved if the number of elements

comprising the particle is increased. Its application to electromagnetic scattering from electrically large and small bodies can be found in the literature [11-13].

Validation of the computational procedures for ε_{eff} has been carried out for uniform ice and water mixtures by Meneghini and Liao [7, 14]. This is done by comparing the scattering parameters from realizations of the mixed-phase particle models with those from a uniform particle with dielectric constant given by ε_{eff}. The results indicate that ε_{eff} , as obtained from (3), is sufficiently accurate that it can be used in calculating the scattering coefficient of uniform mixtures of snow and water for size parameters up to 1. The validation procedure can be extended to the case of 2-layer concentric spheres in which the ice and water are taken as the core (inner sphere) and shell (outer layer) or conversely [15]. Comparisons of scattering parameters between the exact (2-layer concentric sphere) solution [16-17] and the Mie solution for a uniform sphere with the derived effective dielectric constant show the results to be in good agreement for the size parameters up to 1. Further comparisons of the results imply that the ε_{eff} derived from a concentric sphere at a small size parameter (for example, 0.1) is applicable to a uniform sphere model for size parameters up to 1. These findings are consistent with the results found for uniformly mixed ice-water spheres [7]. The independence of ε_{eff} on particle size is of great utility in the application of the ε_{eff} since a single effective dielectric constant can be used for a particular wavelength and water fraction as long as the size parameter of the particle is less than unity.

III. ε_{eff} OF INHOMOGENEOUS MELTING HYDROMETEORS

Fujiyoshi [8] carried out a detailed analysis of melting snowflakes by means of a sequence of photographs of snowflakes at different stages of melting. The observations show that melting

starts at the surface of the particle and gradually progress to the center. These findings are consistent with what Mitra et al. [9] reported in a wind tunnel experiment in their study on melting snowflakes. These findings suggest that an approximate model for the melting snow particle is a non-uniform snow-water mixture where the melt water is concentrated more heavily near the particle boundary. To further simplify the model, the snow particle is taken to a sphere so that the background snow density and the radial distribution of melt water completely specify its composition. Establishing the melting snow model consists of two steps: 1) determination of ε_{eff} for dry snow, the host or background medium and 2) computation of ε_{eff} for melting snow.. The discussion given below starts with an analysis of the results for dry snow followed by computations of ε_{eff} for snow-water mixtures..

A Dry snow (ice-air mixture)

Dry snow can be modeled as an air-ice sphere with a fractional ice content that is generally expressed as a function of radius. In the computations, several trial functions were used to specify the fractional ice content with radius. It was found that the effective dielectric constant derived from (4) using the CGFFT numerical method depends almost entirely on the average mass density of the particle and is nearly independent of the radial variation in ice density. The real and imaginary parts of the effective dielectric constant as determined from the CGFFT and several mixing formulas are displayed in Fig. 1 as functions of the ice fraction. To compare with the measurements of the effective dielectric constants (real part) made by Matzler [18] for dry snow utilizing a special designed resonator operating at a frequency of around 1 GHz [19], the results of Fig.1 are computed at 1 GHz. Note that to better satisfy the boundary conditions at the interfaces of air and ice (or snow and water in the following section), the minimum sizes of any elements of inclusion and matrix should be least 4^3 cells [7]. It is also worth mentioning that the

dielectric constant of snow is insensitive to the frequency in microwave range, up to at least 10 GHz. The measured data (filled circles) shown in Fig.1 are taken from the fit of the measured data. It can be seen that the CGFFT results compare well with results from the mixing formulas of Bruggeman [6] and Maxwell-Garnet [5] either with air matrix and ice inclusion (MG_{ai}) or ice matrix and air inclusion (MG_{ia}). (For the Maxwell-Garnet mixing formula, the 1st and 2nd subscripts represent the components of mixture used as matrix and inclusion, respectively; the letters "a", "i", "s" and "w" represent air, ice, snow and water, respectively.) The results from both the uniform and non-uniform CGFFT models and the Bruggeman mixing formula yield the best agreement with the measurements (real part). We conclude that the effective dielectric constant of dry snow with a non-uniform radial distribution of ice is well approximated by that derived from the uniform mixture and, furthermore, that the CGFFT and the standard mixing formulas yield similar results. In the remainder of the paper, dry snow will be modeled simply as a uniform mixture of air and ice, which will be regarded as the matrix or background medium for computation of melting snow.

B. Melting snow (snow-water mixture)

To simulate the radar echo in the melting layer, a spherical melting snow particle, as described previously, is modeled as a non-uniform mixture in which the fractional water content is given as a function of the radius of the sphere. To model the water distribution, an exponential function is employed to express the fractional water content f_w in terms of radius r:

$$f_w(r) = f_w(0)e^{\beta r}, \qquad r \le r_0, \tag{5}$$

where r_0 is the radius of the particle, $f_w(0)$ is the fractional water content at the center of sphere, and β is the coefficient of the exponent in units of mm^{-1}. Since $f_w(r)$ can not exceed 1, the above equation is valid only if the f_w is less than 1 for $r \le r_0$. This is generally the case where the melting

is in the early to middle stage. In the later stages of melting where the fractional water volume becomes large, $f_w(r)$ can exceed 1 if (5) is used. To prevent this, (5) is modified to

$$f_w(r) = \begin{cases} f_w(0)e^{\beta r}, & r \le r' \\ 1, & r_0 \ge r > r' \end{cases}, \tag{6}$$

where r' is the radius, at which f_w is equal to 1, i.e., $f_w(r')=1$. Note that β specifies the radial gradient of the water fraction so that a larger β results in a more rapid transition from snow to water. Extreme cases are provided by the uniform mixture ($\beta=0$) and the concentric sphere ($\beta=\infty$). When the radius of sphere is divided into n concentric layers of constant thickness, $f_w(0)$ can be solved for a given β, based on the following equation:

$$\sum_{i=1}^{n} f_w(r_i)\delta V_i = F_w V , \tag{7}$$

where δV_i is the volume of the ith layer between radii r_{i-1} and r_i; F_w and V are the overall water fraction and volume of the particle, respectively. It should be noted that finding r' in (6) generally requires an iterative procedure because of the nonlinear nature of (6) and (7).

Shown in Fig.2 are realizations of melting spherical snow particles for water fractions from 0.1 to 0.9 with β set to 4.5 mm^{-1}. The particles are represented as collections of 64x64x64 cubic cells. We have found that the selection of β of 4.5 mm^{-1} gives simulated profiles of air/space-borne radar bright band that are fairly consistent with the measurements. The fractional water contents are also plotted in terms of the radius.

Computing the average internal electric fields by the CGFFT and then using (3) and (4) gives the effective dielectric constants of the particles depicted in Fig.2. In Fig. 3 the real and imaginary parts of ε_{eff} for a frequency of 13.8 GHz (the frequency of the TRMM Precipitation Radar) are plotted versus water fraction for the particles depicted in Fig. 2. The uniform

background medium of dry snow is assumed to be of mass density 0.1 g/cm^3. Also shown in Fig.3 are the dielectric constants from the Maxwell Garnett and the Bruggeman mixing formulas, the results from the CGFFT for uniform mixtures [7] and the results from a concentric sphere model with a snow core and water shell. All the mixing formula results are bounded by the curves of MG_{ws} and MG_{sw}. In particular, the ε_{eff} for the uniform snow-water mixture is approximately midway between MG_{ws} and MG_{sw} while that for a non-uniform mixture tends to be closer to the MG_{ws} than the MG_{sw}.

IV. MELTING HYDROMETEORS MODELED AS STRATIFIED SPHERE

While the CGFFT numerical method can be used to compute ε_{eff}, the computational procedure is time consuming for models consisting of a large number of cells, such as the examples presented in Fig.2. The computations are particularly lengthy if results are needed for several snow densities or for multiple wavelengths. The task is made more difficult because the results must be averaged over a number of particle realizations for estimates of the average scattered fields. For these reasons, it is desirable to have a simple model that approximates the results from the CGFFT scattering model for radially non-uniform snow-water mixtures. Given these considerations, it is natural to think of the stratified sphere, a sphere composed of multiple layers, where the fractional water content is given as a function of radius. However, before using the multi-layer stratified-sphere model, we need to know how the scattering parameters of interest computed from a stratified sphere compare with those from the CGFFT model for a radially non-uniform melting snow sphere. For this purpose, the stratified-sphere scattering models are constructed, as displayed in Fig.4, so as to represent the same melting structures as the CGFFT scattering models of Fig.2. To make the two models equivalent, with the same radial

gradient of water, the stratified spheres are chosen to be composed of 32 layers of equal thickness. The ε^i_{eff}, denoting the effective dielectric constant at the ith layer of the stratified sphere, is taken to be the effective dielectric constant of a homogeneous snow-water mixture with the same water fraction [7].

Plotted in Fig.5 are the extinction and backscattering coefficients (the most relevant scattering and propagation parameters for radar applications) derived from the stratified sphere and the CGFFT non-uniform spherical model as a function of the water fraction. In the calculations, the size parameter was taken to be 0.1. For reference, the results calculated from the Maxwell Garnett and Bruggeman mixing formulas are also plotted. The results show that the scattering parameters derived from the two models are generally in good agreement despite the fact that the extinction and backscattering coefficients obtained by the CGFFT model are slightly higher than those from the stratified-sphere model. Additional comparisons were made at other particle sizes (not shown) with similar results. These findings indicate that the stratified-sphere model, with ε_{eff} at each layer taken from the uniform mixing results, is approximately equivalent to the non-uniform CGFFT calculations. As such, the stratified sphere can be used to compute the scattering parameters of interest for the radar bright band.

In the following section, we employ the stratified-sphere scattering model to simulate profiles of the radar bright-band profiles as measured by airborne and space-borne radars. As efficient numerical solutions are available for the scattering properties of a stratified sphere [20-21], the radial distribution of water fraction within a melting particle can be described in as fine a scale as needed by increasing the number of layers. We have used a 100-layer stratified sphere that provides a good approximation to the radial distribution of water given by (5) and (6).

V. RADAR BRIGHT BAND SIMULATIONS

A melting layer model provides the melting fractions and fall velocities of hydrometeors as a function of the distance from the 0^0C isotherm. By coupling this information with snow mass density, particle size distribution, and the effective dielectric constants of the mixed phase hydrometeors, the backscattering intensities and attenuation coefficients can be computed from any location within the melting region. In our study, the rain drop size distributions are converted into snow and allowed to fall and melt in accordance with the model described by Yokoyama and Tanaka [22]. Aggregation and drop breakup are not included in the model used here.

A. TRMM Precipitation Radar

The TRMM Precipitation Radar (PR), operating at a single frequency of 13.8 GHz, measures precipitation from space [23]. Figure 6 shows an example of measurements from the TRMM PR radar reflectivity on Nov. 18, 1999 at nadir incidence over stratiform rain. The data are taken from version 5 of the TRMM standard product 1C21 [24]. Instead of using only the normally sampled data, which are provided at a range resolution of 250 m, we interleave the normal and over-sampled data so that the range resolution improves to 125 m. With a higher vertical resolution the radar bright band can be profiled in greater detail. A time-average of the data in Fig. 6 yields the radar reflectivity factor profile shown by the thick dotted line in Fig. 7 where only that portion of the profile within and near the melting layer is displayed. The 125-meter resolution data are represented on the plot by filled circles.

As there is only a single measurable (the radar reflectivity factor at 13.8 GHz) at each gate, the single-parameter Marshall-Palmer raindrop size distribution N(D) in $mm^{-1}m^{-3}$ [25] is assumed. This can be expressed as a function of rain rate, R in mm/h, by

$$N(D) = 8000\exp(-4.1R^{0.21}D), \tag{8}$$

where D is diameter of particle in units of mm. The most common form of the Z-R relation, assuming the Marshal Palmer drop size distribution, is given by

$$Z = 200R^{1.6}. \tag{9}$$

At the range just below the melting layer, N(D) is obtained from the measured Z using (8) and (9). To maintain constant mass transport during fall of hydrometeors, the mass flux (the product of N(D) and particle velocity v(D)) is fixed over the regions of snow, melting and rain. This, in turn, provides estimates of N(D) in the snow and melting layers. Once N(D) has been specified throughout the melting layer, the radar reflectivity factor is determined at any range within the melting layer from the following equation:

$$Z = \frac{\lambda^4}{\pi^5 |K_w|^2} \int_0^\infty N(D)\sigma_b(D,\lambda)dD, \tag{10}$$

where $\sigma_b(D,\lambda)$ is the backscattering cross section and λ the radar wavelength. K_w, the dielectric factor, is used to designate $(m^2-1)/(m^2+2)$, where m is the complex refractive index of water. By convention, $|K_w|^2$ is taken to be 0.93. The computations of σ_b depend upon the scattering model of hydrometeors and mixing formulas used in the determination of the effective dielectric constant of melting snow. The melting layer model of Yokoyama and Tanaka [22] is used to produce a table that provides the water fractions and fall velocities of particles at each size bin as a function of distance from 0 ^{0}C isotherm. Using various mixing formulas and hydrometeor's melting models to calculate σ_b in (10), the simulated radar profiles in the melting layer are produced and then compared with the TRMM PR measurements, as shown in Fig.7. The simulated profiles shown in the figure were generated by using the effective dielectric constants derived from the multi-layer

stratified-sphere model, the two-layer concentric sphere (with water shell and snow core), the Maxwell-Garnett [5] and Bruggeman [6] mixing formulas, and the CGFFT uniformly-mixed (snow and water) sphere. Note that the snow mass density is set to 0.1 g/cm^3. Also note that the radar signal attenuation in the melting layer is accounted for so that the simulated radar reflectivity profiles include attenuation effects. It is clear from the results of Fig.7 that the profiles of the radar bright-band derived from the Maxwell-Garnett formulas are either considerably higher (in the case of MG_{ws}) or lower (in the case of MG_{sw}) than the measured profile. Like the MG_{ws} result, the two-layer concentric model produces results that significantly overestimate the measured radar reflectivity. Although the profiles generated by the Bruggeman formula and CGFFT uniform model are relatively close to the measurement, their maxima are 2 to 3 dB lower than the measurement. Of the mixing formulas and particle models considered, the multi-layer stratified-sphere model gives the best agreement with the PR measurement. Not only does it accurately reproduce the intensity of the bright band peak but also it achieves the best overall agreement in the melting region.

B. Dual-Wavelength Airborne Radar

A down-looking airborne radar with good range resolution provides a powerful means to study the melting layer. Utilization of dual-wavelength airborne radar will greatly enhance our ability not only to validate the models but also to improve our understanding of microphysical properties of melting hydrometeors. Figure 8 presents measurements made by the CRL (Communication Research Laboratory of Japan) dual-wavelength airborne radar operating at X and Ka bands (10 and 35 GHz), over stratiform rain during the Convection and Precipitation

Electrification Experiment (CaPE) over the central Florida in 1991. A description of the CRL airborne radar has been given by Kumagai et al. [26]. With a vertical sampling of 30 m, the airborne radar is capable of profiling the bright band in fine detail. The two profiles (bottom panels of Fig.8) corresponding to the vertical bars marked on the images at the top of Fig. 8 show the radar echoes from snow, melting region and rain. It has been demonstrated that the snow size distributions, if expressed in exponential form or a Gamma distribution with fixed shape factor, can be estimated from the X and Ka band measurements [27-32]. In principle, if the proper model is used, the measured reflectivity profiles associated with melting region can be reproduced by the simulations with the model inputs of the snow size distribution derived above the melting layer. However, the differences of the radar reflectivity factors in snow between X and Ka bands, which are used for determining the snow size distribution, vary greatly with height, as shown in Fig.8, largely because of snow aggregation. This leads to simulations of the bright band that are highly sensitive to the radar range at which the size distribution is inferred. In fact from an examination of the radar profiles alone it is not obvious where the melting begins.

Unlike the snow region, the radar reflectivities of rain below the melting layer appear fairly stable in spite of the gradual decrease due to rain attenuation. The iterative procedure described here is designed to estimate the raindrop size distribution at a height where the melting process of snow is complete. The raindrop size distribution is then converted to distributions in the snow and melting regions assuming a constant mass flux throughout the melting layer. The procedure can be described mathematically as follows. The melting layer is divided into n equal range gates. The range gates, r_i, i=1, 2, ..., n, are counted downward starting at the 0^oC isotherm. The first gate (i=1) corresponds to a region of dry snow, and the last gate (right after melting is completed) to a region of rain. To express the particle size distribution, an exponential function

is used in snow, melting and rain regions. Thus, the size distribution at the ith gate can be written as

$$N_i(D) = N_0(r_i)\exp\left(-3.67\frac{D}{D_0(r_i)}\right), \tag{11}$$

where N_0 is the coefficient, D_0 the median volume diameter and D the particle diameter. The number concentration, N_T, integral of (11) over all D, at the ith gate can be expressed in terms of these variables by:

$$N_T(r_i) = {}^{N_0(r_i)D_0(r_i)}\!/_{3.67}. \tag{12}$$

For the sake of consistency, the D and D_0 are taken to refer to the melted diameter. In light of the dual-wavelength radar techniques [27-32], the D_0, N_0 and specific attenuation coefficients, k in dB/km, can be expressed as

$$\begin{aligned} &D_0(r_i) = p_i(DFR(r_i)) \\ &N_0(r_i) = q_i(D_0, Z_e^{(1)}(r_i)) \\ &k^{(1)}(r_i) = u_i(D_0, N_0) \\ &k^{(2)}(r_i) = v_i(D_0, N_0) \\ &i = 1,2,...,n \end{aligned}, \tag{13}$$

where

$$DFR = Z_e^{(1)} - Z_e^{(2)}, \tag{14}$$

p, q, u and v are known functions, which depend on the distance from the 0°C level, and Z_e is the true (i.e., unattenuated) radar reflectivity factor in dB. The superscripts (1) and (2) stand for the 1st and 2nd frequencies of the dual-wavelength radar. We begin with the $D_0(r_n)$ and $N_0(r_n)$, which are estimated from (13) by letting

$$\begin{aligned} &Z_e^{(f)}(r_n) = Z_m^{(f)}(r_n) \\ &f = 1,2 \end{aligned}, \tag{15}$$

as the initial guesses, where Z_m is apparent or measured reflectivity. Keeping the constant mass flux throughout the melting layer, as assumed in the melting layer model, requires

$$N(D)v(D) = C, \tag{16}$$

where C is a constant and v(D) is the fall velocity of the particle of diameter of D, and given by the melting layer model. Thus, the N(D) is obtained by

$$\begin{aligned} &N_i(D) = N_n(D)v_n(D)/v_i(D) \\ &i = 1,2,...,n \end{aligned} \tag{17}$$

Utilizing the scattering and melting layer models along with the N(D) from (17), the attenuation coefficients can be calculated at each gate. The path attenuation, A_n, from the radar to the nth gate is

$$\begin{aligned} &A_n^{(f)} = 2\sum_{i=1}^{n} k^{(f)}(r_i)\Delta r \\ &f = 1,2 \end{aligned}, \tag{18}$$

where Δr is the radar range resolution. The factor of 2 in (18) accounts for the 2-way path attenuation. Correcting the measured reflectivity factors at the nth gate by the path attenuations given in (18), we have

$$\begin{aligned} &Z_e^{(f)}(r_n) = Z_m^{(f)}(r_n) + A_n^{(f)} \\ &f = 1,2 \end{aligned} \tag{19}$$

As a result, new $D_0(r_n)$ and $N_0(r_n)$ are obtained from (13) .This completes the first iteration. The procedure is then repeated until the differences in the $D_0(r_n)$ and $N_0(r_n)$ between the current and previous steps are smaller than a predefined value. The flow chart in Fig. 9 shows how this iterative procedure is used to derive the D_0 and N_0 of the rain.

Applying this procedure to the measured profiles depicted in Fig.8, the radar profiles are simulated, as illustrated in Fig.10 and 11, at 3 snow densities by using the scattering parameters

from the statified-sphere model in conjunction with the derived snow size distributions. Analysis of the results indicates that the simulated and measured profiles are generally in good agreement. The profiles generated for a snow density of 0.05 g/cm^3 yield the best comparisons to the measurements. The comparisons also indicate that the agreement at X band is better that at Ka band, a fact that might be attributable to multiple scattering effects at Ka band, an effect which is not included in the model [33-35]. Table 1 displays the final results of D_0 and N_T for snow and rain for the estimated radar bright-band profiles shown in Figs.10 and 11 for snow densities of 0.05, 0.1 and 0.2 g/cm^3. Because of differences of particle fall velocities between snow and rain, the number concentrations of snow particles are about 4 times greater than the concentrations of raindrops. The values of D_0 in rain are slightly smaller than in snow. It should be mentioned that the iterative procedure described here and illustrated in Fig.9 does not converge if the Maxwell-Garnett mixing formula or the concentric-sphere is used. Moreover, if the ε_{eff} derived from the CGFFT for a uniform snow-water mixture or the Bruggeman mixing formula is used, we find large discrepancies between the measured and simulated X and Ka band bright-band profiles.

Because of the different scattering characteristics at X and Ka bands, faithful reproduction of the measured profiles at both frequencies is much more challenging than reproduction at a single frequency. The variation in the results obtained from different dielectric constants is substantial even in the case of a single frequency. For the dual-frequency case, the simulation succeeds in consistently obtaining agreement with measured profiles only when the stratified sphere model is used.

The fact that the stratified-sphere scattering model best reproduces the dual-wavelength radar measurements suggests that the non-uniformly melting scattering model may be appropriate for radar simulations of the bright band. Nevertheless, the simulated profiles, based on our results

from a number of simulations, are in good agreement with the measurements for the TRMM PR and dual-wavelength radar only if β of (5) and (6) is selected to be approximately 4 mm^{-1}. As described earlier, values of β much higher than 4 mm^{-1} results in a more rapid transition from snow to water within the particle, making the particle similar to a concentric sphere with water in the outer layer. At X-band, this leads to an overshoot of the peak of the bright band and an underestimate of the overall profile of the melting layer at Ka band because of enhanced attenuation. In addition, use of a larger β alters the shapes of the radar profiles in the melting region in the sense that the location of the peak tends to move closer to the 0°C isotherm. As β is decreased from a value of 4 mm^{-1}, the radial gradient of the melt water becomes weaker and ultimately tends toward a uniform snow-water mixture. For these cases the peak reflectivity is smaller than the measurements. It is found that the optimum choice of β is relatively insensitive to snow density used in the model. In the absence of observations, the functional form of (5) and (6) and the specific value of β can not be validated. Moreover, if significant aggregation occurs in the melting layer, an effect which is not accounted for in the particle melting model used here, a reduction in the value of β would be needed to obtain good agreement with the measured data. Despite these deficiencies, the model provides a fairly general way to compute the scattering characteristics of radially non-uniform melting snow spheres and moreover, yields good agreement with both single and dual-frequency measurements. Improvements in calculating the scattering properties of mixed phase (water-snow) particles must advance along two paths: 1) more extensive observations of melting particles; 2) more accurate scattering calculations for these particle along with accurate effective dielectric constants that capture their essential scattering features. For analysis of cross-polarized returns in the melting layer, the spherical

particle model is obviously inadequate; possible generalizations would be a stratified spheroidal particle model with a scalar ε_{eff} or a stratified sphere with a tensor effective dielectric constant.

VI. SUMMARY

The internal electric field of mixed phase particles can be used to calculate an effective dielectric constant, ε_{eff}. In this paper, we have done this by first dividing the particle into 64^3 equi-volume cells and then using the Conjugate-Gradient and Fast-Fourier Transform techniques to solve for the internal field. Previous work along these lines [7,14] focused on computations of ε_{eff} for uniform mixtures where the probability of ice, air or water is independent of location within the particle. As shown in the first part of the paper, an effective dielectric constant also can be computed for cases where the fractional water or ice content varies with radius. In the case of an ice-air mixture, it was found that radial gradients in the fractional ice content have only a negligible effect on ε_{eff} and that the scattering properties of the dry snow mixture depend almost exclusively on particle mass. On the other hand, for a snow-water sphere, the radial gradient in the fractional water content has a strong influence on the particle scattering properties. The CGFFT numerical methods can be used to compute ε_{eff} for radially non-uniform snow-water mixtures. However, the computational requirements are formidable. To simplify the problem, it has been shown that the particle model can be replaced by a multi-layer stratified sphere where the ε_{eff} at the ith layer is obtained from CGFFT-derived value of ε_{eff} for a uniform mixture with the same fractional water/snow content.

As an application of the result, the stratified sphere model for non-uniform melting snow was used to generate radar bright-band profiles. The simulated profiles were compared with data from the TRMM PR at 13.8 GHz and from dual-wavelength airborne radar data at 10 GHz and 35 GHz. For the TRMM PR, the Marshall-Palmer raindrop size distribution was used as input to

the melting layer model. For the dual-wavelength case, an iterative procedure was applied to the data to determine the parameters of the size distribution in rain, which were then used to generate the bright band profiles at both frequencies. The results show that the simulated bright-band profiles are in good agreement with the measurements and suggest that the proposed particle scattering model can provide reasonable agreement with both single and dual-wavelength radar measurements.

As with nearly all radar simulations of the melting layer, there are a number of free parameters that must be assumed in the calculations. These include snow density, effects of drop aggregation and break-up, and various assumptions included in the particle melting model. In our case, the quantity β, which determines that radial gradient of water within the melting particles, is an additional free parameter whose value was chosen to yield the best agreement with the radar measurements. High-resolution images of melting particles and theoretical work that yield details on the distribution of melt water within the particle will be needed to determine this parameter independently. Another deficiency in the particle model is its restriction to spheres. While non-spherical particles are essential for understanding cross-polarization effects, it can be argued that for co-polarized measurements of the radar reflectivity at near-nadir incidence, particle shape is a second-order effect. Nevertheless, an extension of the theory of effective dielectric constants to non-spherical mixed phase particles would be useful not only in radar polarimetric applications but in microwave radiometry as well.

References

[1] W. S. Olson, P. Bauer, N. F. Viltard, D. E. Johnson, W.-K. Tao, R. Meneghini, and L. Liao, "A melting-layer model for passive/active microwave remote sensing applications. Part I: Model formulation and comparison with observations," *J. Appl. Meteor.*, vol. 40, pp. 1145-1163, 2001.

[2] W. S. Olson, P. Bauer, C. D. Kummerow, Y. Hong, and W.-K. Tao, "A melting-layer model for passive/active microwave remote sensing applications. Part II: Simulations of TRMM observations," *J. Appl. Meteor.*, vol. 40, pp. 1164-1179, 2001.

[3] F. Fabry and W. Szyrmer, 1999: Modeling of the melting layer. Part II: Electromagnetics. *J. Atmos. Sci.,* vol. 56, pp. 3596-3600, 1999.

[4] Bringi, V. N., R. M. Rasmussen, and J. Vivekanandan, "Multiparameter radar measurements in Colorado convective storms. Part I: Graupel melting studies," *J. Atmos. Sci.,* vol. 43, pp. 2545-2563, 1986.

[5] J. C. Maxwell Garnett, "Colours in metal glasses and in metallic films," *Philos. Trans. Roy. Soc. London,* vol. 203A, pp. 385-420, 1904.

[6] D. A. G. Bruggeman, "Berechnung verschiedener physikalischer Konstanten von heterogenen Substanzen: I. Dielectrizitatskonstanten und Leitfahigkeiten der Mischkorper aus isotropen Substanzen," *Ann. Phys.,* vol. 24, pp. 636-679, 1935.

[7] R. Meneghini and L. Liao, "Effective dielectric constants of mixed-phase hydrometers," *J. Atmos. Oceanic Technol.,* vol. 17, pp. 628-640, 2000.

[8] Y. Fujiyoshi, "Melting snowflakes," *J. Atmos. Sci.,* vol. 43, 307-311, 1986.

[9] S. K. Mitra, O. Vohl, M. Ahr, and H. R. Prupappacher, "A wind tunnel and theoretical study of the melting behavior of atmospheric ice particles. Part IV: Experiment and theory for snow flakes," *J. Atmos. Sci.*, vol. 47, 584-591, 1990.

[10] D. Stroud and F. P. Pan, "Self-consistent approach to electromagnetic wave propagation in composite media: application to model granular metals," *Phys. Rev. B.*, vol. 17, 1602-1610, 1978.

[11] T. K. Sarkar, E. Arvas, and S. M. Rao, "Application of FFT and the conjugate gradient method for the solution of electromagnetic radiation from electrically large and small conducting bodies," *IEEE Trans. Antennas Propag.*, vol. AP-34, pp. 634-640, 1986.

[12] L. Liao and K. Sassen, "Investigation of relationships between Ka-band radar reflectivity and ice and liquid water contents," *Atmos. Res.*, vol. 34, pp. 231-248, 1994.

[13] M. F. Catedra, R. P. Torres, J. Basterrechea and E. Gago, *The CG-FFT Method: Application of Signal Processing Techniques to electromagnetic.* Artech House, 361 pp., 1995.

[14] R. Meneghini and L. Liao, "Comparisons of cross sections for melting hydrometeors as derived from dielectric mixing formulas and a numerical method," *J. Appl. Meteor.*, vol. 35, pp. 1658-1670, 1996.

[15] L. Liao and R. Meneghini, "A study of effective dielectric constant of ice-water sphereswhere fractional water content is prescribed as a function of radius," Preprints 29th Conf. Radar Meteor., American Meteor. Soc., 699-702, 1999.

[16] A. L. Aden and M. Kerker, "Scattering of electromagnetic waves by two concentric spheres," *J. Appl. Phys.*, vol. 22, pp. 1242-1246, 1951.

[17] K. Aydin and Y. Zhao, "A computational study of polarimetric radar observables in hail," *IEEE trans. Geosci. Remote Sens.*, vol. 28, pp. 412-422, 1990.

[18] C. Matzler, "Microwave permittivity of dry snow," *IEEE trans. Geosci. Remote Sens.*, vol. 34, pp. 573-580, 1996.

[19] C. Matzler, "Applications of the interaction of microwaves with the natural snow cover," *Remote Sensing Rev.*, vol. 2, pp. 259-392, 1987.

[20] Z. P. Wu and Y. P. Wang, "Electromagnetic scattering for multilayered sphere: Recursive algorithms," *Radio Sci.*, vol. 26, pp. 1391-1401, 1991.

[21] N. V. Voshchinnikov and J. S. Mathis, "Calculating cross sections of composite interstellar grains," *Astrophys. J.*, vol. 526, pp. 257-264, 1999.

[22] T. Yokoyama and H. Tanaka, "Microphysical process of melting snowflakes detected by two-wavelength radar," *J. Meteor. Soc. Japan*, vol. 62, pp. 650-666, 1984.

[23] T. Kozu et al., "Development of precipitation radar onboard the Tropical Rainfall Measuring Mission (TRMM) Satellite," *IEEE Geosc. Remote Sensing*, vol. 39, pp. 102-116, 2001.

[24] T. Iguchi, T. Kozu, R. Meneghini, J. Akawa and K. Okamoto, "Rain-profiling algorithm for TRMM precipitation radar," *J. Appl. Meteor.*, vol. 39, pp. 2038-2052, 2000.

[25] J.S. Marshall and W.M. Palmer, "The distribution of raindrops with size," *J. Meteor,* vol. 5, pp.165-166, 1948.

[26] H. Kumagai, R. Meneghini, and T. Kozu, "Preliminary results from multiparameter airborne rain radar measurement in the western Pacific," *J. Appl. Meteor.*, vol. 32, pp. 701-711, 1994.

[27] R. Meneghini, T. Kozu, H. Kumagai, and W. C. Boncyk, " A study of rain estimation methods from space using dual-wavelength radar measurements at near-nadir incidence over ocean," *J. Atmos. Oceanic Technol.*, vol. 9, pp. 364-382, 1992.

[28] S. Y. Matrosov, " Radar reflectivity in snowfall," *IEEE Trans. Geosci. Remote Sens.*, vol. 30, pp. 454-461, 1992.

[29] L. Liao, L., R. Meneghini, T. Iguchi and A. Detwiler, "Estimation of snow parameters from dual-wavelength airborne radar," Preprints 28th Conf. Radar Meteor., American Meteor. Soc., 510-511, 1997.

[30] R. Meneghini, H. Kumagai, J. Wang, T. Iguchi and T. Kozu, "Microphysical retrievals over stratiform rain using measurements from an airborne dual-wavelength radar-radiometer," *IEEE Trans. Geosci. Remote Sens.*, vol. 29, pp. 690-703, 1997.

[31] S. Y. Matrosov, "A dual-wavelength radar method to measure snowfall rate," *IEEE Trans. Geosci Remote Sens.*," vol. 30, pp. 454-461, 1998.

[32] R. Mardiana, T. Iguchi, and N. Takahashi, "A dual-frequency rain profiling method without the use of a surface reference technique," *IEEE Trans. Geosci Remote Sens.*," vol. 42, pp. 2214-2225, 2004.

[33] A. Ishimaru, R. Woo, J. W. Armstrong, and D. C. Blackman, "Multiple scattering calculations of rain effects," *Radio Sci.*, vol. 17, pp. 1425-1433, 1982.

[34] A. Tsolakis, and W. L. Stutzman, "Multiple scattering of electromagnetic waves by rain," *Radio Sci.*, vol. 17, pp. 1495-1502, 1982.

[35] S. Ito, T. Oguchi, T. Iguchi, H. Kumagai, and R. Meneghini, "Depolarization of radar signals due to multiple scattering in rain," *IEEE Trans. Geosci Remote Sens.*," vol. 33, pp. 1057-1062, 1995.

Table 1 Final values of D_0 and N_T of snow and rain for the radar simulated profiles given in Figs.15 and 16 for 3 snow densities. D_0 of snow is denoted as the melted median volume diameter.

ρ (g/cm^3)	D_0 (Fig.15/Fig.16), mm		N_T (Fig.15/Fig.16), mm^{-3}	
	Snow	Rain	Snow	Rain
0.05	1.49/1.65	1.39/1.52	5637/5065	1174/1092
0.1	1.37/1.54	1.31/1.46	7981/6432	1769/1456
0.2	1.39/1.54	1.35/1.48	5675/4957	1403/1296

Table captions

Table 1. Final values of D_0 and N_T of snow and rain for the radar simulated profiles given in Figs.15 and 16 for 3 snow densities. D_0 of snow is denoted as the melted median volume diameter.

Figure captions

Fig. 1 Comparisons of real (top) and imaginary (bottom) parts of ε_{eff} of air-ice mixed spheres as derived from the CGFFT and the mixing formulas as a function of ice fraction at a frequency of 1 GHz. The measurement data (filled circles) of the real part [18] are also shown in the top panel for the ice fraction up to 0.5.

Fig. 2 Realizations of snow-water particles where the fractional water content is given as a function of radius.

Fig. 3 Plots of real (top) and imaginary (bottom) parts of ε_{eff} of snow-water spheres versus water fractions at a frequency of 13.8 GHz (TRMM PR frequency). The computations are made for a snow density of 0.1 g/cm^3.

Fig. 4 Stratified sphere models of melting snow for volume-averaged water fraction, F_w, from 0.1 to 0.9. The radial distribution of water, f_w, varies with radius and with F_w in the same manner as the realizations in Fig.2.

Fig. 5 Stratified sphere and CGFFT results for the extinction (top) and backscattering (bottom) coefficients of non-uniform melting snow versus water fraction. The computations are made at a size parameter of 0.1. For reference, the results from Maxwell-Garnet and Bruggeman's mixing formulas are included.

Fig. 6 Measurements of the TRMM PR radar reflectivity for stratiform rain at nadir incidence on Nov. 18, 1999 with vertical resolution of 125 m. Both normal and oversampled data are taken from TRMM product 1C21.

Fig. 7 Comparisons of the averaged TRMM PR profile of radar reflectivity factor with simulations derived from several models for the effective dielectric constant of mixed phase hydrometeors.

Fig. 8 Measurements of the X and Ka band radar reflectivity factors for stratiform rain (top), and vertical radar reflectivity profiles (bottom) at the distances marked on the upper images.

Fig.9 Flow chart outlining the backward iterative procedures for simulations of dual-wavelength radar returns in melting layer.

Fig.10 Profiles of radar reflectivity factor at X (top set) and Ka (bottom set) bands simulated from the stratified-sphere model at snow densities of 0.05, 0.1 and 0.2 g/cm^3. Also shown are the measured profiles (left-hand side) from Fig.8.

Fig.11 Same as Fig.10, but for the measured radar reflectivity profiles shown on the right-hand side of Fig.8.

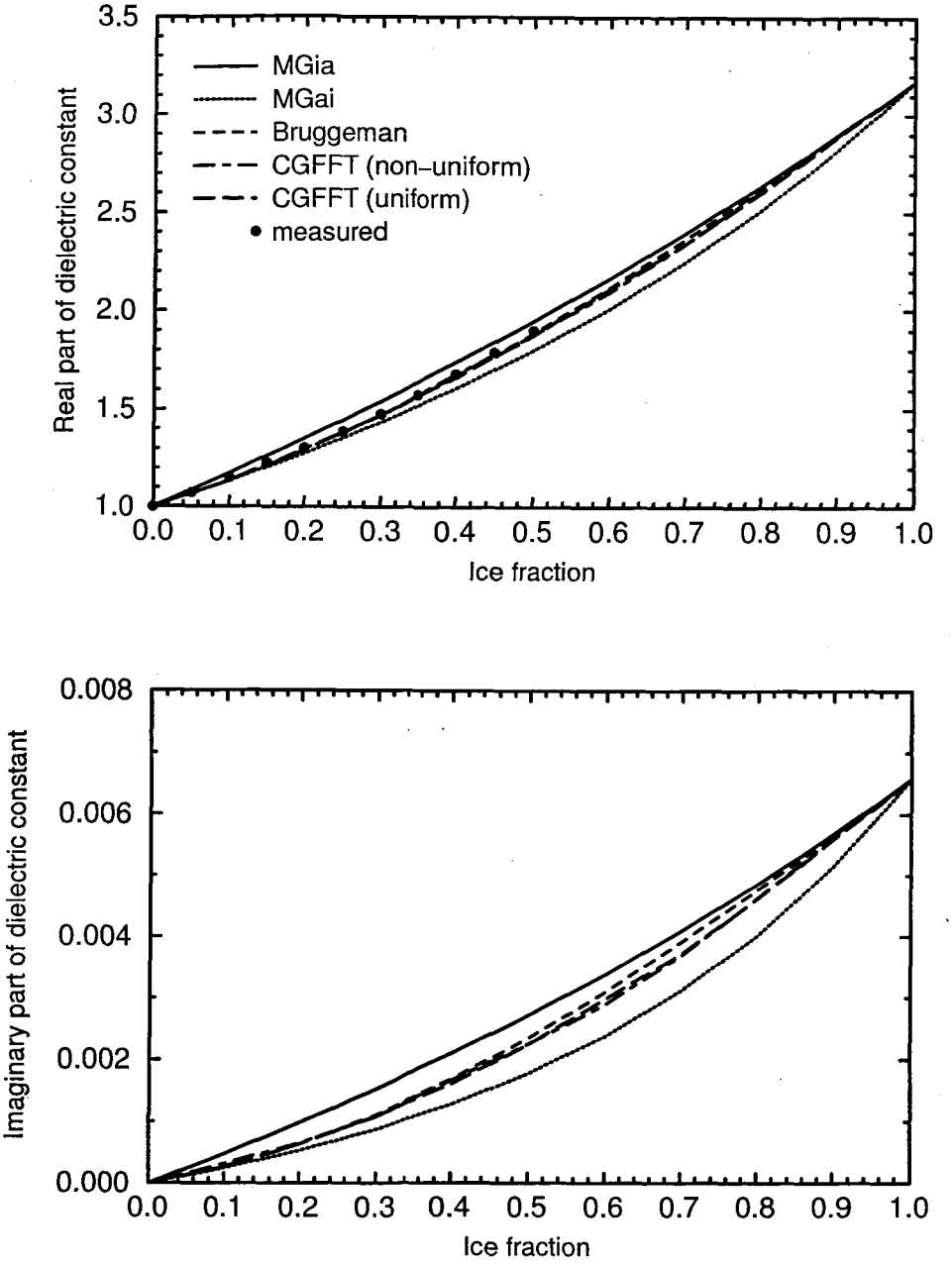

Fig.1 Comparisons of real (top) and imaginary (bottom) parts of ε_{eff} of air-ice mixed spheres as derived from the CGFFT and the mixing formulas as a function of ice fraction at a frequency of 1 GHz. The measurement data (filled circles) of the real part [18] are also shown in the top panel for the ice fraction up to 0.5.

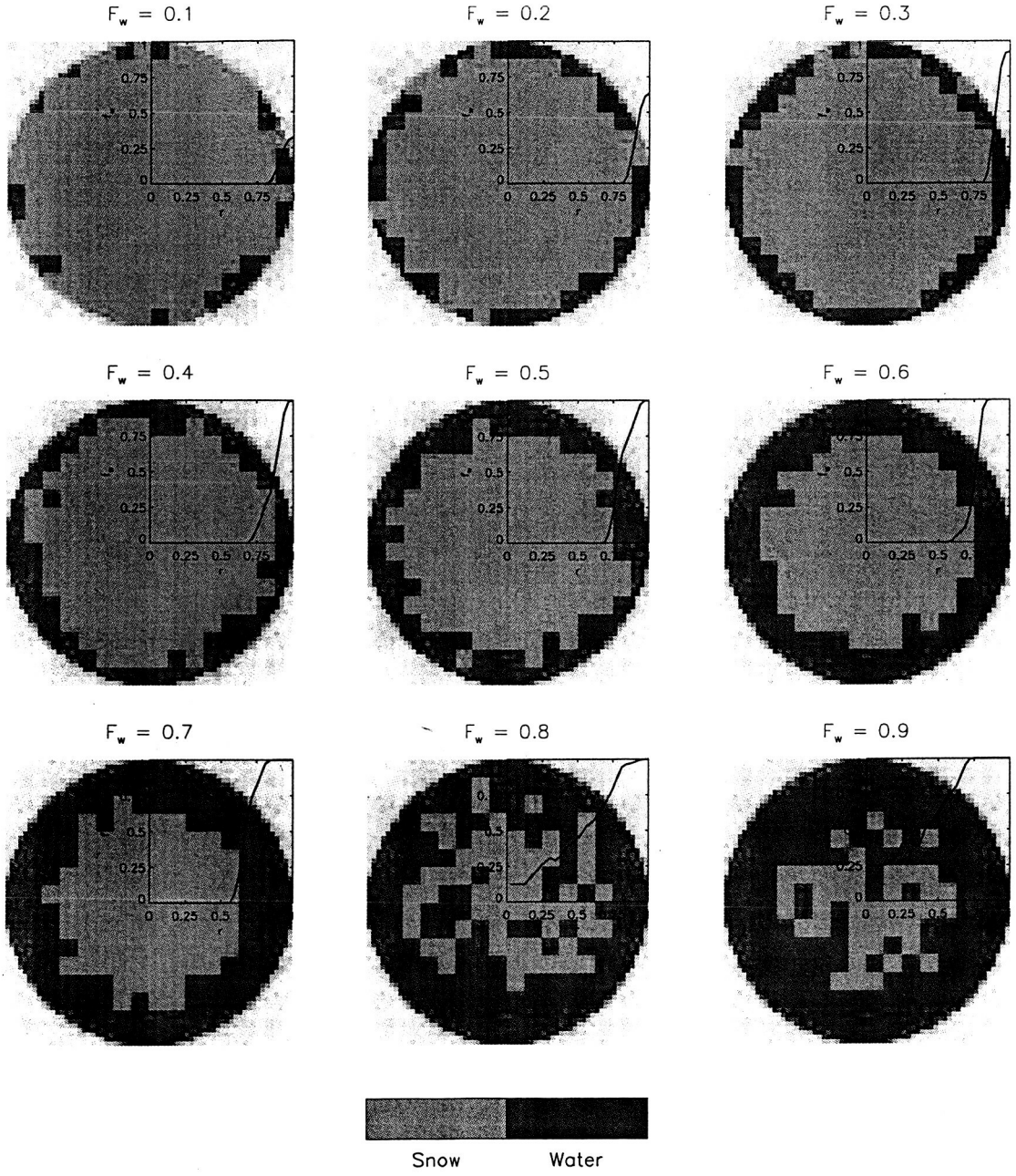

Fig.2 Realizations of snow-water particles where the fractional water content is given as a function of radius.

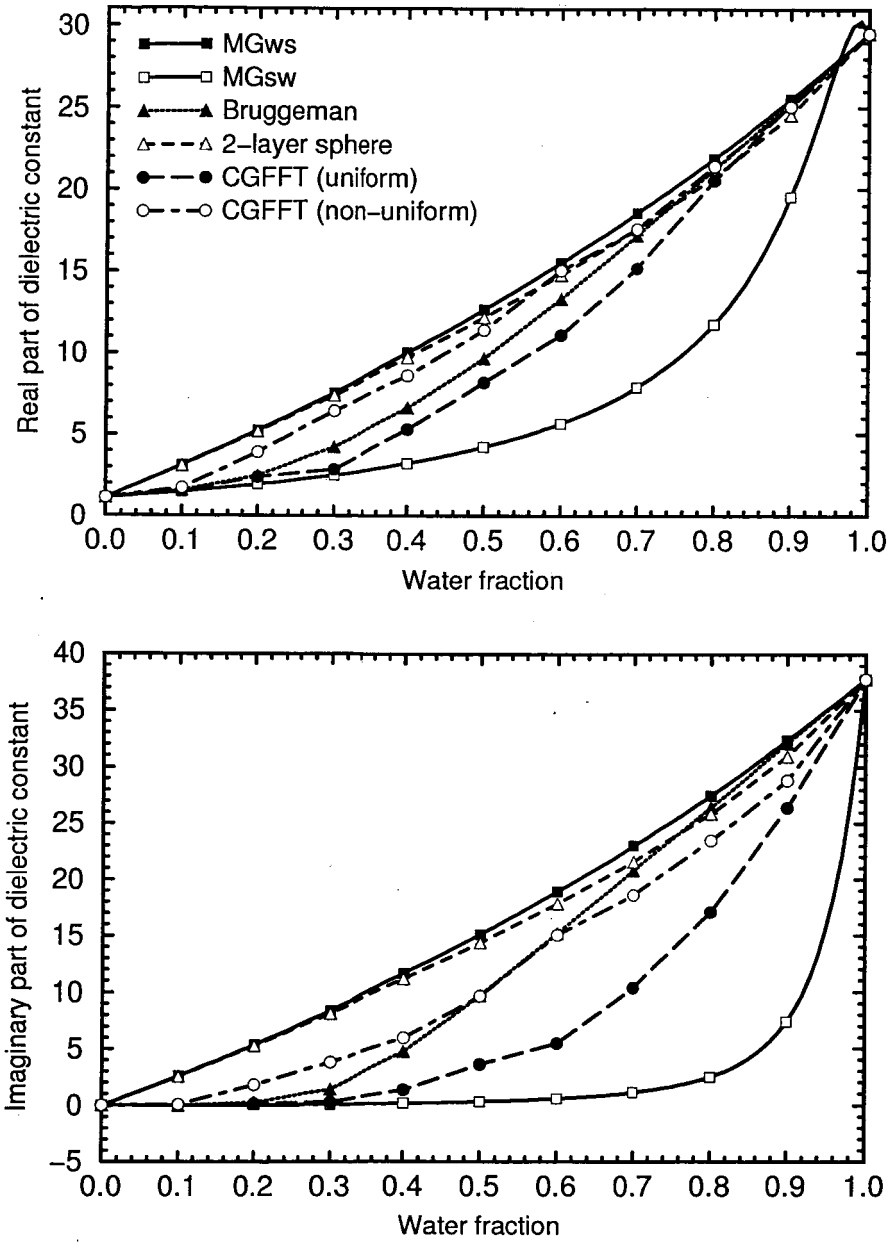

Fig. 3 Plots of real (top) and imaginary (bottom) parts of ε_{eff} of snow-water spheres versus water fractions at a frequency of 13.8 GHz (TRMM PR frequency). The computations are made for a snow density of 0.1 g/cm^3.

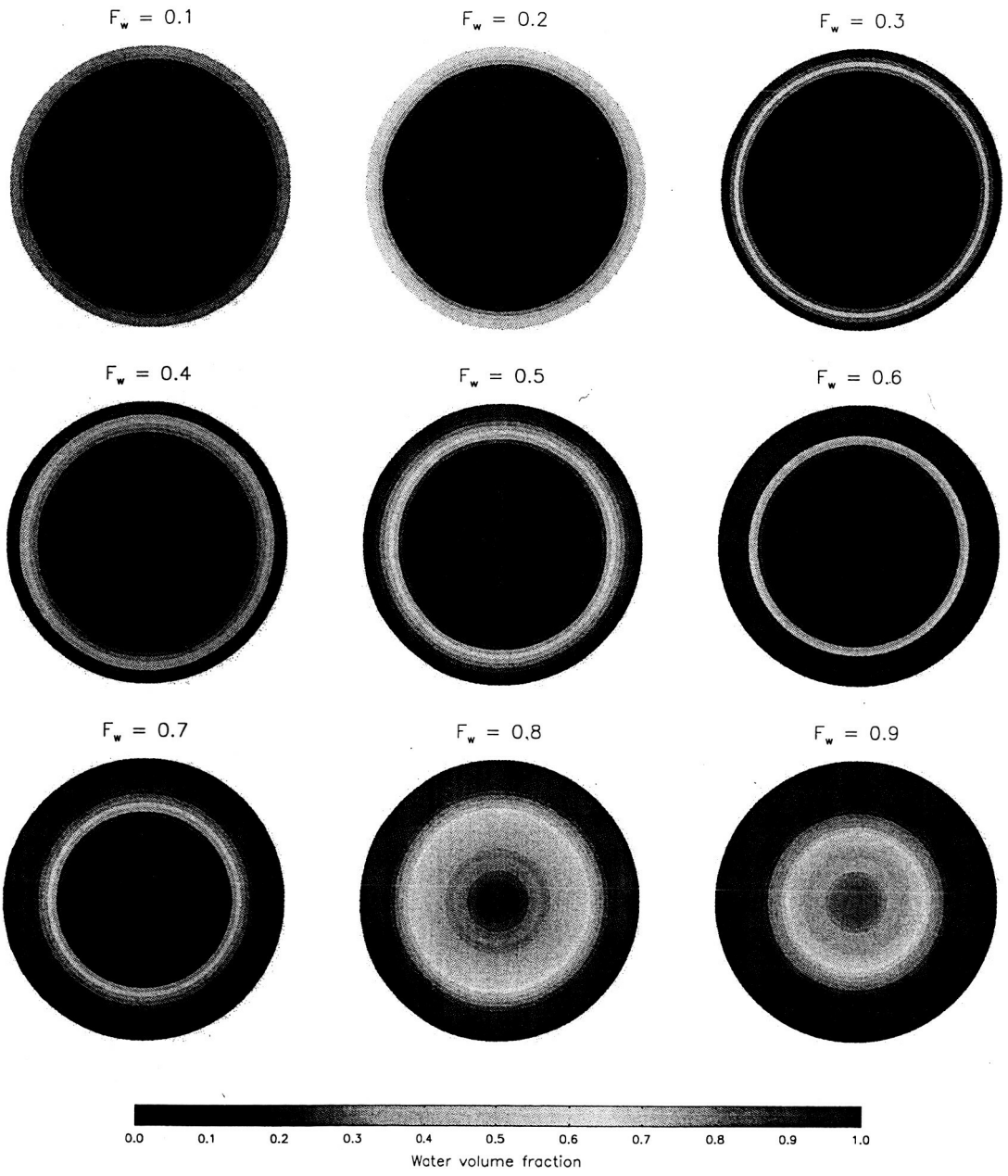

Fig.4 Stratified sphere models of melting snow for volume-averaged water fractions, F_w, from 0.1 to 0.9. The radial distribution of water, f_w, varies with radius and with F_w in the same manner as the realizations in Fig. 2.

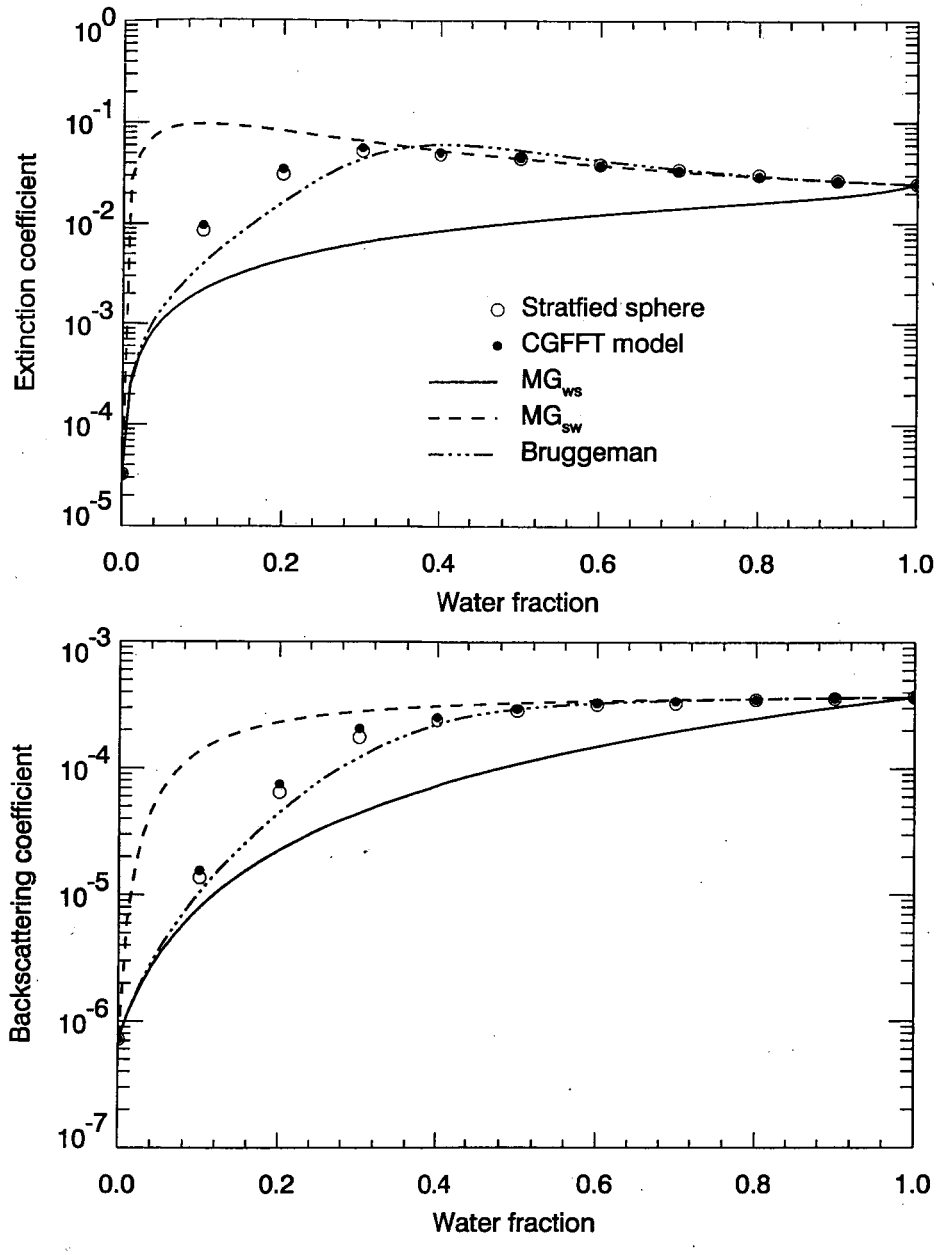

Fig.5 Stratified sphere and CGFFT results for the extinction (top) and backscattering (bottom) coefficients for non-uniform melting snow versus water fraction. The computations are made at a size parameter of 0.1. For reference, the results from Maxwell-Garnet and Bruggeman's mixing formulas are included.

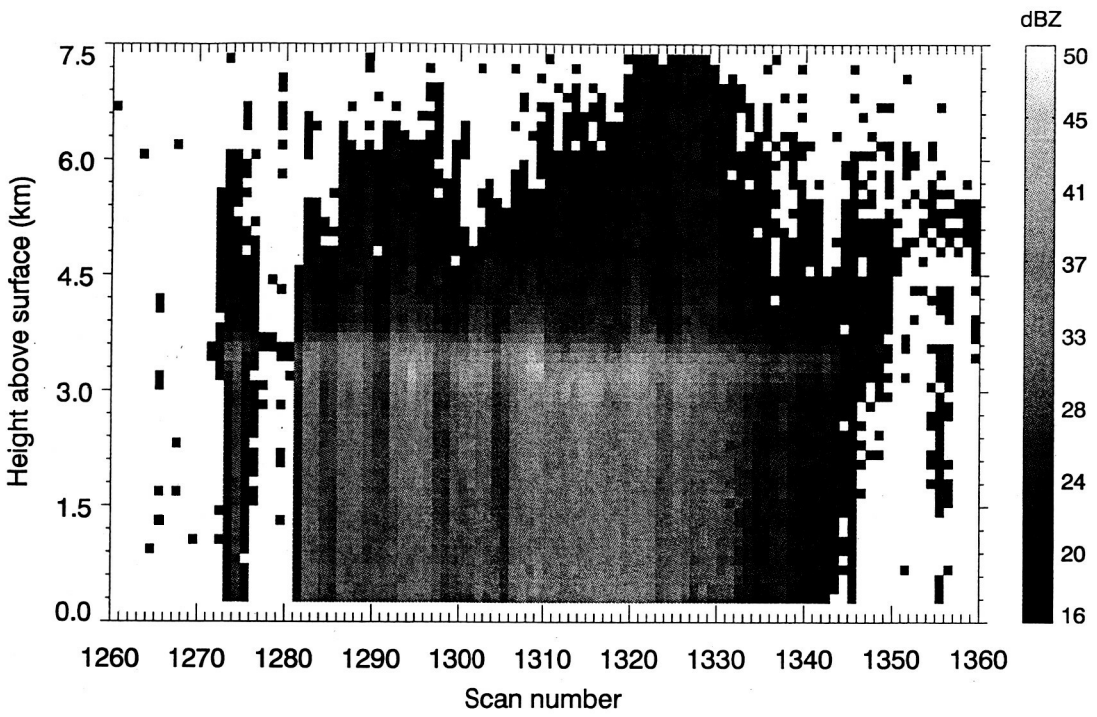

Fig.6 Measurements of the TRMM PR radar reflectivity factor for stratiform rain at nadir incidence on Nov. 18, 1999 with vertical resolution of 125 m. Both normal and oversampled data are taken from TRMM product 1C21.

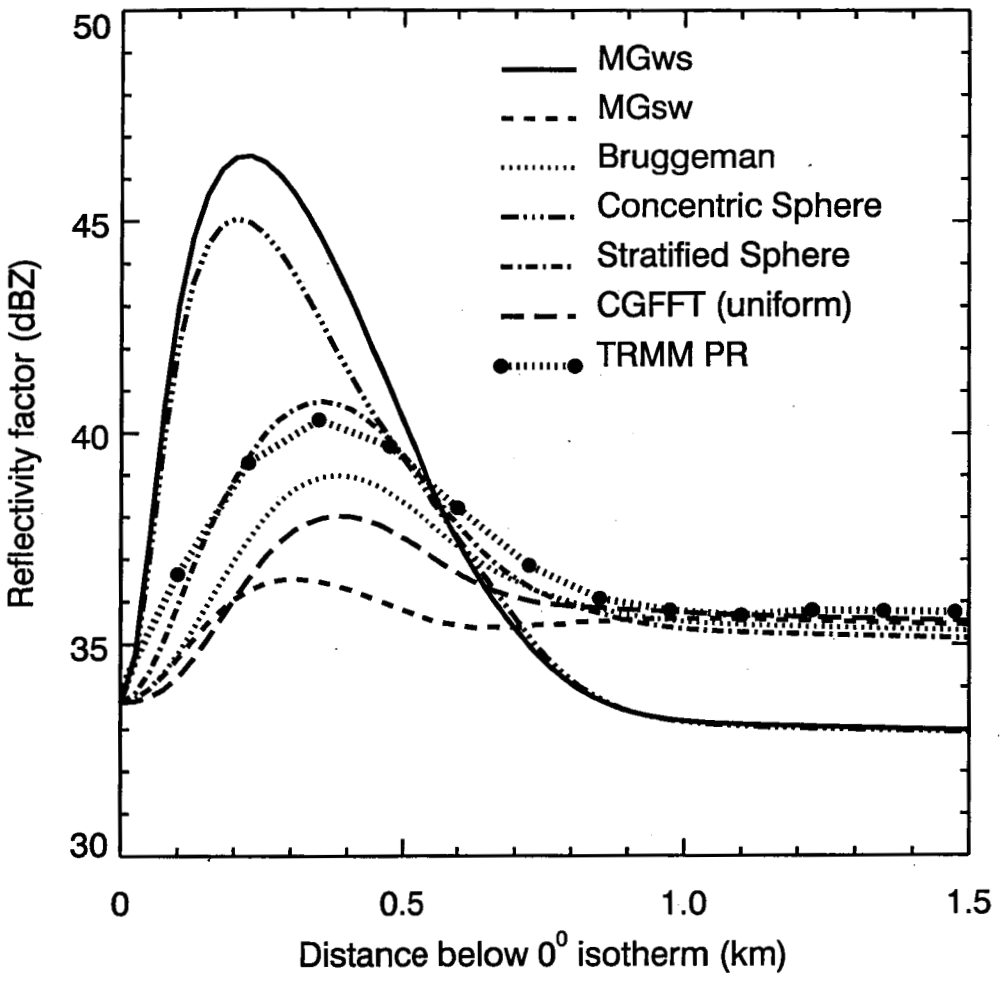

Fig.7 Comparisons of the averaged TRMM PR profile of radar reflectivity factor with simulations derived from several models for the effective dielectric constant of mixed phase hydrometeors.

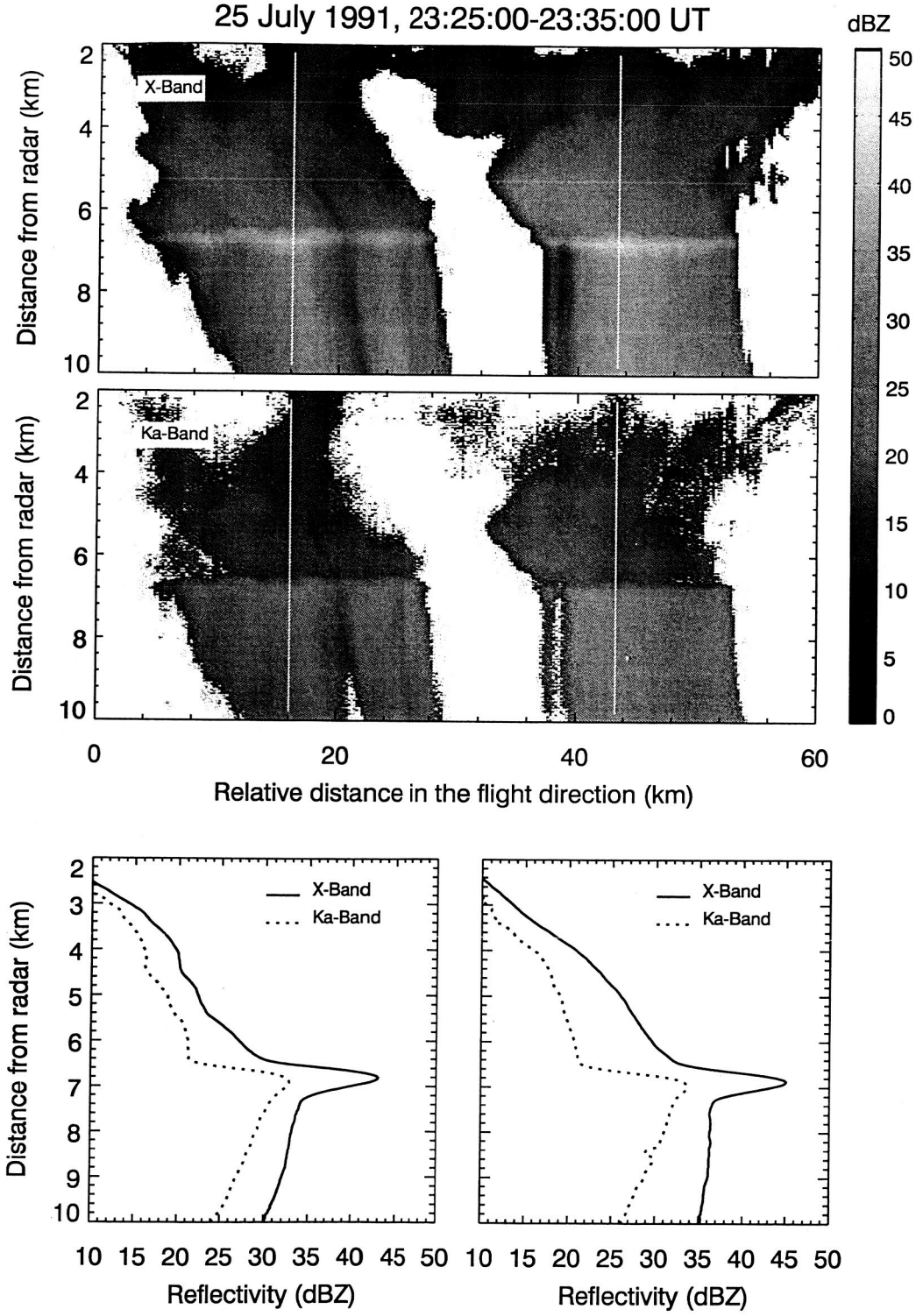

Fig.8 Measurements of the X and Ka band radar reflectivity factors for stratiform rain (top), and vertical radar reflectivity profiles (bottom) at the distances marked on the upper image.

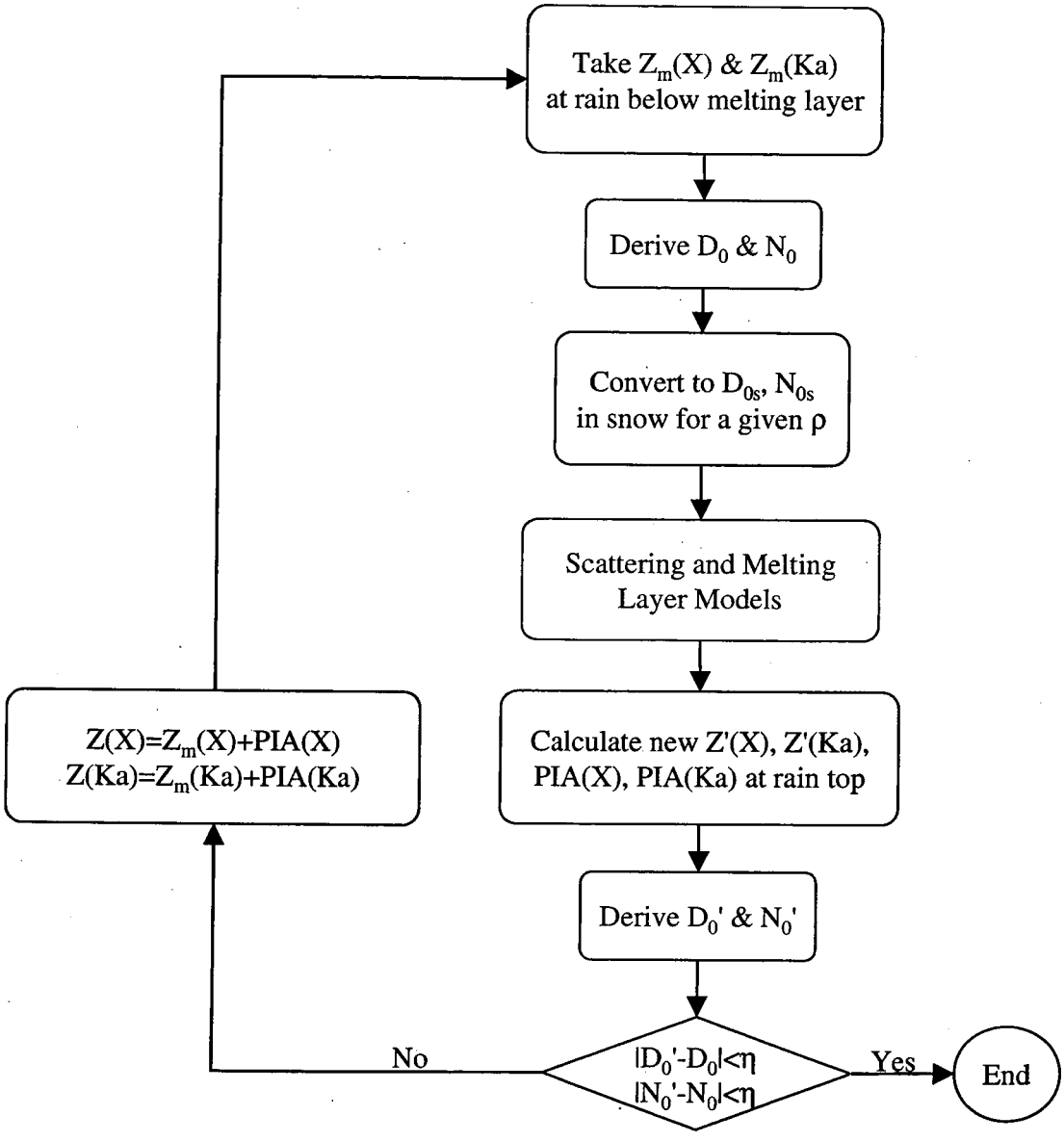

Fig.9 Flow chart outlining the backward iterative procedures for simulations of dual-wavelength radar returns in melting layer.

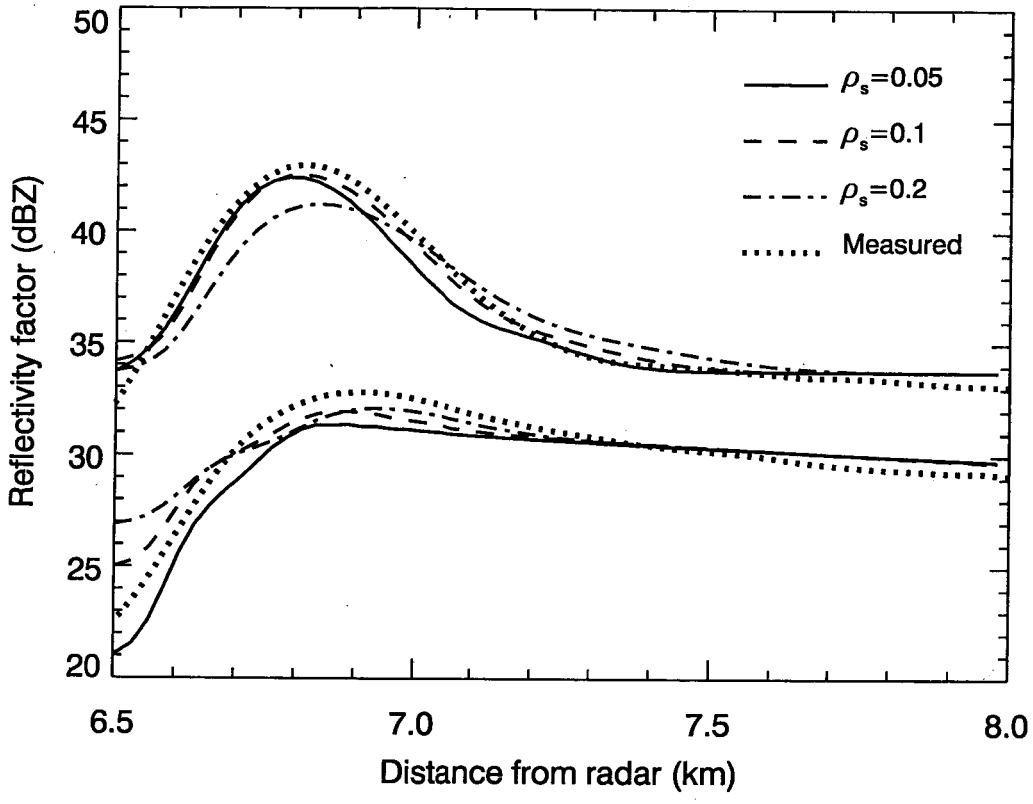

Fig.10 Profiles of radar reflectivity factor at X (top set) and Ka (bottom set) bands simulated from the stratified-sphere model at snow densities of 0.05, 0.1 and 0.2 g/cm^3. Also shown are the measured profile (left-hand side) from Fig.8.

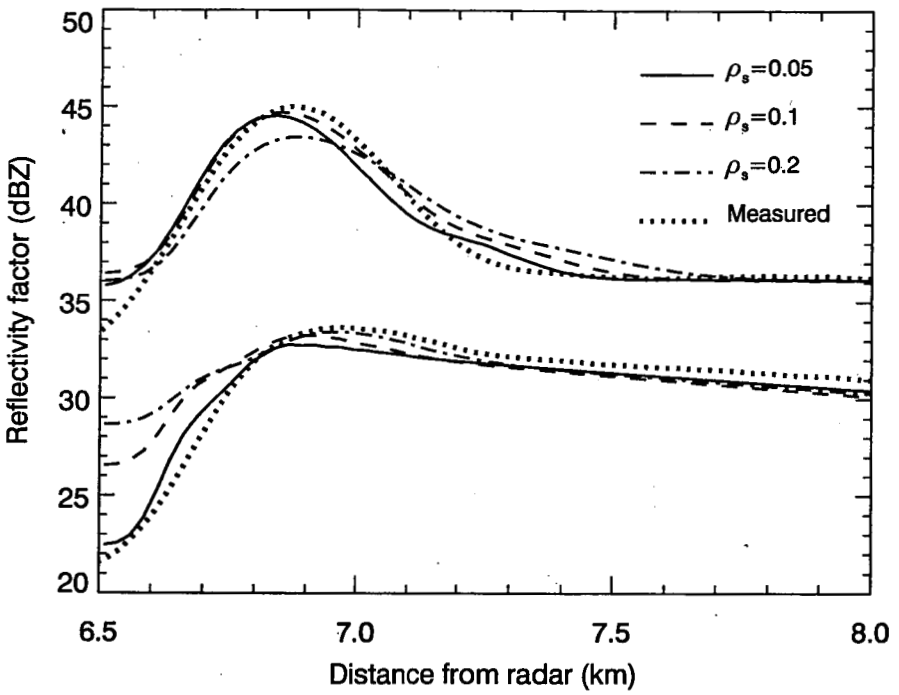

Fig.11 Same as Fig.10, but for the measured reflectivity profiles shown on the right-hand side of Fig.8.